RSC Advances

PAPER

View Article Online
View Journal | View Issue

Cite this: *RSC Adv.*, 2025, **15**, 13712

Synergistic efficiency of modified banana leaf derived cellulose-g-C_3N_4 hybrid composite: a sustainable approach for visible-light-driven photodegradation of dyes†

Priyanka P. Mishra,[a] Diptiranjan Behera,[a] Sushree Suman,[a] Nigamananda Das,[a] Bankim C. Tripathy,[b] Jagadish Kumar[c] and Ajaya K. Behera *[a]

The adverse effects on human health and water supplies due to widespread use of dyes including methylene blue (MB) and rhodamine B necessitate their removal. Photocatalytic decontamination offers an alternative method which is cost effective and ecofriendly compared to other costly dye removal processes. The combination of graphitic carbon nitride (g-C_3N_4) and cellulose from readily available modified banana leaves (MBLC) has not been explored for color degradation. The present work investigates the application of a promising g-C_3N_4–MBLC composite for the photocatalytic removal of methylene blue and rhodamine B dyes. The two-component hybrid composite was synthesized utilizing the one-pot *in situ* thermal polymerization techniques. Furthermore, multiple analytical methods were exploited to comprehensively assess the structural and morphological characteristics of the synthesized g-C_3N_4–cellulose hybrid composite. The composites exhibited photocatalytic activity, successfully degrading 93.35% of RhB and 92.06% (30 mg L^{-1}) of MB dyes within 120 minutes under visible irradiation. Analysis of scavenging effects indicated that $^{\bullet}O_2^-$ and h^+ radicals were the primary reactive oxygen species (ROS) responsible for the photodegradation of the dyes. Additionally, the synthesized composite showed excellent reusability, maintaining 81% efficiency after five consecutive cycles, highlighting its potential for practical applications, particularly in pollutant removal.

Received 17th February 2025
Accepted 24th April 2025

DOI: 10.1039/d5ra01156f

rsc.li/rsc-advances

1. Introduction

The current era's substantial industrial expansion and population surge have triggered a worrisome escalation in environmental contamination, posing significant risks to human well-being and ecological systems.[1] Global catastrophes have been sparked by the accumulation of extensive waste from textile and dyeing sectors, encompassing organic dyes, heavy metals, and other hazardous compounds.[2] Contemporary investigations reveal that textile industries release an estimated 40 000–50 000 tons of diverse dyes into aquatic ecosystems.[3,4] The chemical structure of these dye structures can transform the chemical and physical attributes of water bodies, thus jeopardizing human health and environmental integrity. Rhodamine B (RhB), an artificial dye classified under the xanthene category, is extensively employed across various sectors. It is regularly utilized in biotechnology applications, incorporated into cosmetic formulations, and employed as a coloring agent in food products, notably in spices like curry and chili powder. The European Food Safety Authority (EFSA) later prohibited the use of this substance due to its resistance to degradation and its harmful effects on both humans and animals, including neurotoxicity, chronic toxicity, and carcinogenicity.[5,6] This necessitates the treatment of wastewater containing this dye before its discharge into aquatic ecosystems. In a similar vein, methylene blue (MB), a highly carcinogenic cationic thiazine dye, finds widespread application in various industries, such as textile dyeing, paper coloring, hair dyeing, and as a redox indicator in space. MB consumption can lead to severe health complications, including nervous system

[a]*Department of Chemistry, Utkal University, Bhubaneswar, Odisha 751004, India. E-mail: ajayabehera@utkaluniversity.ac.in; Fax: +91 0674 2581850; Tel: +91-9938956715*

[b]*Hydro & Electrometallurgy Department, CSIR-Institute of Minerals and Materials Technology, Bhubaneswar 751013, Odisha, India*

[c]*Department of Physics, Utkal University, Bhubaneswar, Odisha 751004, India*

† Electronic supplementary information (ESI) available: Fig. S1: XPS spectral scan of 'C 1s' of MBLC. Fig. S2 Graphical representation of changes in HOMO–LUMO gaps, HOMO and LUMO of MBLC, Fig. S3(a) Nitrogen adsorption–desorption isotherms and (b) pore size distribution curves of g-C_3N_4, g-C_3N_4/C-MBLC, Fig. S4(a) Linear plot of Freundlich isotherm model, and (b and c) Linear plots of pseudo-second-order kinetic models respectively at different initial dye concentrations, Fig. S5: Zeta potential graph of g-C_3N_4/C-MBLC composite. Fig. S6: FTIR assessment using g-C_3N_4/C-MBLC composite. See DOI: https://doi.org/10.1039/d5ra01156f

and ocular damage, nausea, diarrhea, vomiting, respiratory issues, and gastric inflammation.[7] Consequently, there is a pressing need for advanced techniques to remove these hazardous contaminants from water sources.

In the realm of wastewater purification, adsorption has emerged as a prominent method, surpassing other techniques due to its high efficiency, cost-effectiveness, and economic advantages.[8,9] Nevertheless, conventional adsorbents frequently encounter obstacles such as constrained surface areas, insufficient absorption capacities, weak chemical stability, and recycling issues. Standard approaches have exhibited limited efficacy in eliminating ionic dyes.[10] Consequently, a tenacious need exists for an environmentally sustainable and energy-efficient wastewater treatment solution. Recently, the advanced oxidation process (AOP) (photocatalysis) has garnered significant attention for its potential in organic dye removal.[11] This eco-friendly innovative technique has found application in wastewater treatment owing to its capacity to fully degrade organic pollutants through the action of superoxide radicals ($^{\bullet}O_2^-$) and hydroxyl radicals ($^{\bullet}OH$).[11] The utilization of active oxygen species and the lack of harmful by-product formation during the degradation process establishes this method as a formidable approach to wastewater treatment.

Photocatalysts are classified into two main types: metal-based and nonmetal-based. Metal-based photocatalysts offer advantages such as exceptional durability and swift reaction rates.[12,13] However, they face challenges in utilizing natural light effectively for photocatalytic processes and may contribute to secondary pollution through heavy metal release.[14] In contrast, non-metallic photocatalysts, including graphitic carbon nitride (g-C_3N_4) and graphene oxide, are economical and environmentally benign.[15] g-C_3N_4 has attracted considerable attention due to its narrow band gap (>2.8 eV), visible light responsiveness, and uncomplicated synthesis methods.[16] Nevertheless, its catalytic properties are hindered by poor dispersion and agglomeration of the nanoscale powder on surfaces. To overcome the limitations of individual photocatalysts, researchers are incorporating g-C_3N_4 into metal-based oxides or biomass materials to enhance their dispersal and improve photocatalytic efficiency.

Biomass materials, such as chitin, chitosan, cellulose, biochar, activated carbon, charcoal, and waste chitin flasks, are increasingly utilized in catalytic applications.[17–19] Chen *et al.*, synthesized g-C_3N_4-cellulose aerogel for photocatalytic degradation of Cr(VI) and antibiotics.[20] Similarly, He *et al.* also fabricated chitin-modified carbon/g-C_3N_4 for the photodegradation of Rhodamine B dye.[21] We opted to derive cellulose from modified banana leaves (MBLC) due to its compatibility with biological systems, eco-friendly characteristics, and capacity to create porous structures. Banana leaves are widely sourced from banana plantations, where they are discarded as byproducts, making them a sustainable and readily available raw material for cellulose extraction. By synthesizing a hybrid composite that includes cellulose, we seek to boost photocatalytic performance by enhancing catalyst distribution, minimizing agglomeration, and simplifying recycling processes. MBLC plays a crucial role in the g-C_3N_4 photocatalytic system by modifying the surface, facilitating charge separation, and enhancing mass transport. The process of electron charge transfer involves photoexcited electrons from g-C_3N_4 to cellulose, where cellulose acts as an electron mediator that improves the breakdown of pollutants. This collaborative effect minimizes recombination and enhances the photocatalytic performance of the composite. This makes it an excellent support material for use in wastewater treatment applications.[20,22] The hydroxyl group on the cellulose surface establishes strong interfacial bonds with g-C_3N_4 *via* hydrogen bonding, which improves the charge migration efficacy and supports the photocatalytic degradation of dyes under visible light, thereby improving the dye removal performance.[23,24] Additionally, minor chemical or physical modifications to cellulose moieties can further increase the number of surface-active sites. Among the various modifications, the carbon derived from cellulose is a viable approach. In this context, Kumar *et al.* also derived carbon from the chitin for the modification of g-CN nanosheets for the effective removal of pollutants.[25] Similarly, Chen *et al.* also utilized the cellulose-derived carbon/g-C_3N_4 complex for the H_2 production and the degradation of tetracycline.[25] However, the disordered movement of the cellulose-derived carbon species in the g-CN nanosheets also bridges a gap for the improvement in the g-CN composite.

In this work, g-C_3N_4/C-MBLC composite has been utilized for the photodegradation of Rhodamine B and methylene blue dyes, where the cellulose was isolated from the modified banana leaves. Due to the abundance of hydroxyl (–OH) groups in the MBLC, they easily interact with the amino (–NH_2) groups in melamine, resulting in the formation of hydrogen bonds. This bonding makes it difficult for the MBLC to detach from the nanosheets during the calcination process. The g-C_3N_4 aggregation is anticipated to be surmounted by using cellulosic carbon species (MBLC) as a photocatalytic carrier, as it improves the migration of charge carriers, which offers numerous potential for the eradication of dyes in the aquatic environment.

2. Materials and methodology

2.1. Materials and chemicals required

Modified banana leaves were obtained from the Utkal University campus, in Bhubaneswar, India. Chemicals like toluene (CAS no. 108-88-3, SRL, India), ethanol (CAS no. 64-17-5, Merck, India), KOH (CAS no. 1310-58-3, Finar, India), acetic acid (CAS no. 64-19-07, Finar, India), rhodamine B (MG, CAS no. 81-88-9, Sigma-Aldrich, India) and methylene blue (MB, CAS no. 122965-43-9) were procured.

2.2. Synthesis of extracted cellulose

The extraction of pure cellulose from modified banana leaves followed a multi-step process (Fig. 1(a)). Initially, the red-colored modified banana leaves (MBL), naturally present in the banana plant, were thoroughly cleansed with deionized water and dried at 50 °C. The dried material was then ground into a powder and sorted using Tyler screens to obtain various

MBL powder fractions. Subsequently, the powder underwent treatment with a 150 mL toluene-ethanol mixture (2 : 1 v/v) to eliminate pigment, wax, and oil, followed by oven drying at 50 °C. The de-waxed powder was then subjected to an 8 hours treatment in a solution of 4 wt KOH and 2 wt% H_2O_2 at 40 °C, followed by 4 hours of heating at 90 °C. After cooling to room temperature, the mixture was filtered and extensively washed with deionized water to remove dissolved substances. The resulting solid sample, dried overnight at 80 °C, was then immersed in 250 mL of acetic acid solution (pH 3–4) at 50 °C for 5 hours. Finally, the mixture underwent centrifugation, air-drying, and repeated rinsing with deionized water until the filtrate achieved a neutral pH. The extracted cellulose was denoted as MBLC (Fig. 1(a)).

2.3. Synthesis of g-C_3N_4/C-MBLC composite

A g-C_3N_4 catalyst was synthesized from melamine by adopting the thermal polymerization method. 10 grams of melamine were heated to 550 °C in a muffle furnace for 2 hours and stored in a closed crucible. After reaching ambient temperature, the bulk product was subjected to rigorous grinding in a mortar. This grinding technique culminated in successfully synthesizing a vivid, yellow-colored substance. The synthesis of the binary composite involves the following procedure.[21,25,26] To synthesize the composite, a homogeneous mixture with 30 mL of deionized water, 0.5 g of extracted cellulose (MBLC), and 1 g of melamine was mixed and swirled in a magnetic stirrer for 3 hours. Then the synthesized precipitate was rinsed several times using distilled water and ethanol and dried overnight at

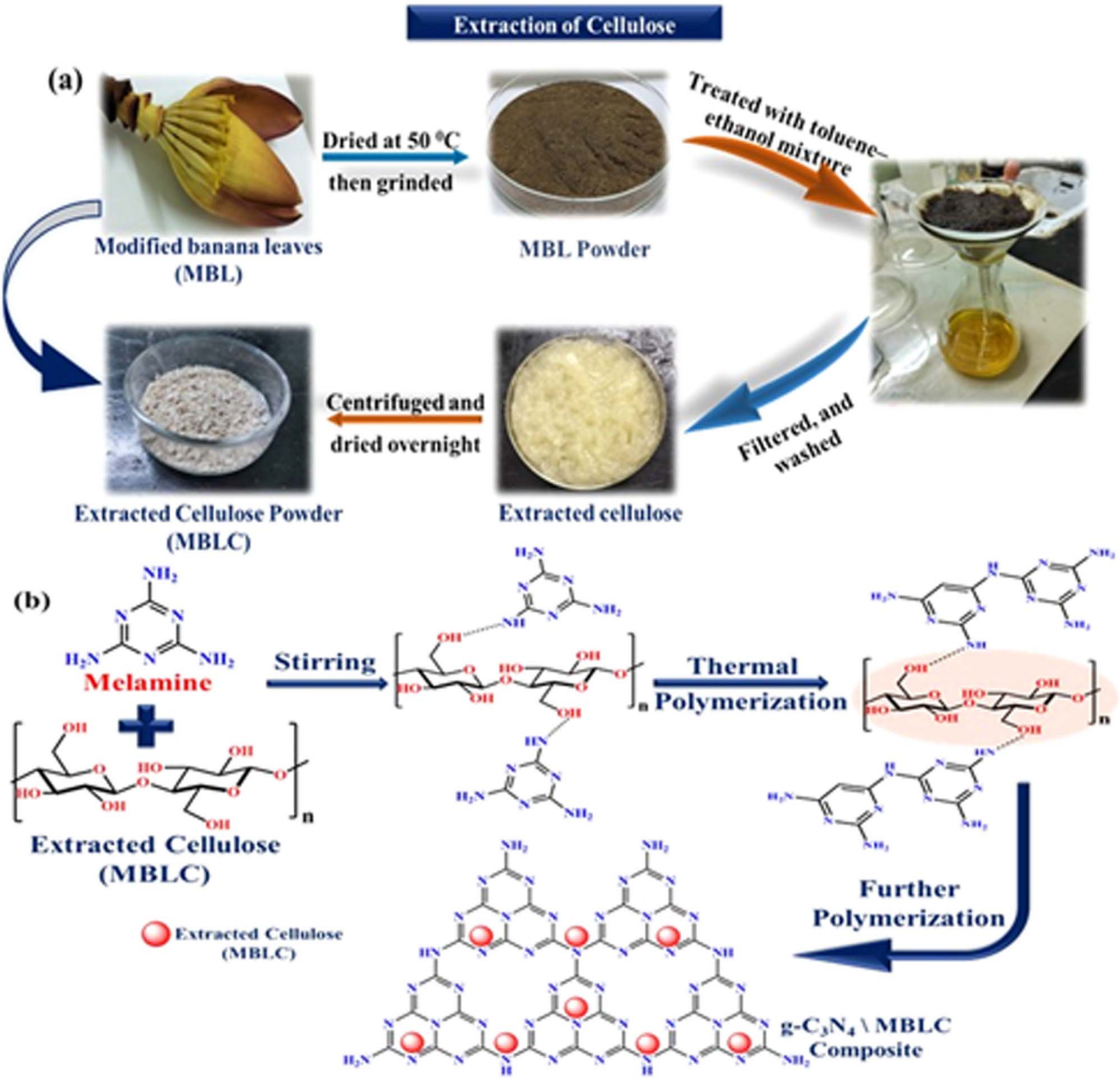

Fig. 1 (a) Extraction of cellulose, (b) synthesis of binary g-C_3N_4/C-MBLC composite.

80 °C. A g-C_3N_4/C-MBLC sample was obtained by calcination for 2 hours at 520 °C (Fig. 1(b)).

2.4. Adsorption and photocatalytic measurement

To evaluate the adsorption capacity of the synthesized nanocomposites, experiments were performed using RhB and MB in aqueous solutions. Dye stock solutions were prepared by dissolving 500 mg of the dye in 1 L of deionized water. Adsorption experiments were conducted in Erlenmeyer flasks with dye concentrations ranging from 10 to 70 mg L^{-1}, while maintaining a constant adsorbent dosage of 100 mg. A measured quantity of adsorbent was added to 100 mL of dye solution, and the mixture was agitated at 320 rpm in a temperature-controlled water bath. At regular intervals, 5 mL samples of the dye solution were extracted and centrifuged. The spectral characteristics of these aliquots were analysed using a PerkinElmer UV-visible spectrometer.

$$q_e = \frac{(A_0 - A_t)}{W} \times V \quad (1)$$

where A_0 and A_t refer to dye concentrations (mg L^{-1}) at times 0 and t, respectively, q_e is the optimum sorption capacity (mg g^{-1}); V (ml) and W (g) are the whole volume of the solution is the mass of sorbent.

To assess the photocatalytic efficacy of the experimental-synthesized material, rhodamine B and methylene blue were applied as water pollutants. Using a 125 W mercury lamp (2.60 mW cm^{-2}) as a source of illumination, a predetermined quantity of g-C_3N_4/C-MBLC was added to 150 mL of dye solution in a photocatalytic reactor to examine the photocatalytic degradation of cationic dyes over the prepared catalytic materials.[4] To prevent the minor UV radiation from the lamp source, a 0.1 M $NaNO_2$ aqueous solution was circulated in the reactor's outer jacket. The experiment was carried out by varying the concentration of dyes from 10–70 mg L^{-1} at a photocatalytic dosage of 100 mg. Then, the dye solution and catalytic material were subjected to mechanical stirring, and 5 mL of the sample solution was collected and centrifuged at regular intervals, spanning from 0 to 120 minutes. A magnetic stirrer was positioned in the center throughout the experiment to ensure a uniform solution. Utilizing a PerkinElmer UV-visible spectrometer, the residual concentration of the mixture was ascertained at λ_{max} = 543 nm for rhodamine B and 664 nm for methylene blue, respectively. The removal percentage of dyes was calculated using the formula as follows:

$$\text{Degradation } (\%) = \frac{(A_0 - A_t)}{A_0} \times 100 \quad (2)$$

Herein, A_0 and A_t are the initial and optimum concentrations of dyes w.r.t time t.

2.5. Characterisation

The structural properties of the pure and synthesized samples were examined using X-ray diffraction (XRD) patterns, obtained with a Philips-PW 1800 diffractometer employing Cu Kα radiation (λ = 1.54186 Å). Functional analysis was carried out using a Shimadzu IRAffinity-1S instrument in KBr medium. A Zeiss EVO microscope, operating at 25 kV acceleration voltage, was used for scanning electron microscopy (SEM) to analyze elemental compositions, surface morphology, and detect elements. The optical energy band gap was determined through UV-visible diffuse reflectance (UV-Vis-DR) spectroscopy, with spectra recorded using a Shimadzu UV-2400 UV spectrophotometer. The analysis of photocatalytic degradation products was performed using gas chromatography-mass spectrometry (GC-MS) measurements on an Agilent 5977B instrument with electrospray ionization mass spectrometry, providing information about the configuration and transformation of the degradation products.

2.6. Theoretical analysis using density functional theory (DFT)

Using the ORCA 5.0 program, DFT calculations were conducted with the hybrid B3LYP/g function and a def2/J, def2/SVP basis set. This method optimized the molecular geometry of MBLC, g-C_3N_4, and the g-C_3N_4/C-MBLC composite. The HOMO and LUMO interactions were visualized using Avogadro 1.2.0 software. To calculate the adsorption energies (E_{ad}) of optimized samples, the same basis set and theory level were applied, as shown in eqn (3).[27]

$$E_{ad} = E_{\text{g-}C_3N_4/\text{C-MBLC}} - (E_{\text{g-}C_3N_4} + E_{MBLC}) \quad (3)$$

Here, $E_{\text{g-}C_3N_4/\text{C-MBLC}}$, $E_{\text{g-}C_3N_4}$, and E_{MBLC} denote the adsorption energies of the g-C_3N_4/C-MBLC composite, g-C_3N_4, and MBLC composite units, respectively.

3. Results and discussion

3.1. Structural analysis

Using XRD analysis, the crystalline arrangements of g-C_3N_4, extracted cellulose (MBLC), and g-C_3N_4/C-MBLC were investigated between 10° and 80°, as shown in Fig. 2(a). The (100) and (002) crystal planes of g-C_3N_4 are responsible for the peak intensity for 2θ values of 12.95° and 27.25°, respectively.[28] This further supports the presence of aromatic delocalization of g-C_3N_4. The (110), (200), and (004) crystal planes of extracted cellulose (MBLC) are attributed to the major diffraction peaks at 16.3°, 22.6°, and 34.8°. The MBLC crystalline phase is verified by the 100% peak intensity at 22.6°.[29] Comparable diffraction peaks of cellulose and g-C_3N_4 were seen in the composite, further confirming the successful formation of the material. The lack of a distinctive cellulose peak in the g-C_3N_4/C-MBLC composite is likely due to the minimal presence of cellulose within the composite structure. Additionally, the enhanced crystallinity observed in the (002) plane of the composite suggests that the cellulose component's interaction with g-C_3N_4 leads to an increase in the crystalline nature of g-C_3N_4.[21]

Fig. 2(b) illustrates the FTIR spectra of the pristine samples and the synthesized composite. In the case of g-C_3N_4, the aromatic ring and the stretching vibrations of C–N and C=N heterocycles are represented by multiple peaks ranging between 1230 and 1610 cm^{-1}, while the sharp band at 808 cm^{-1} denotes

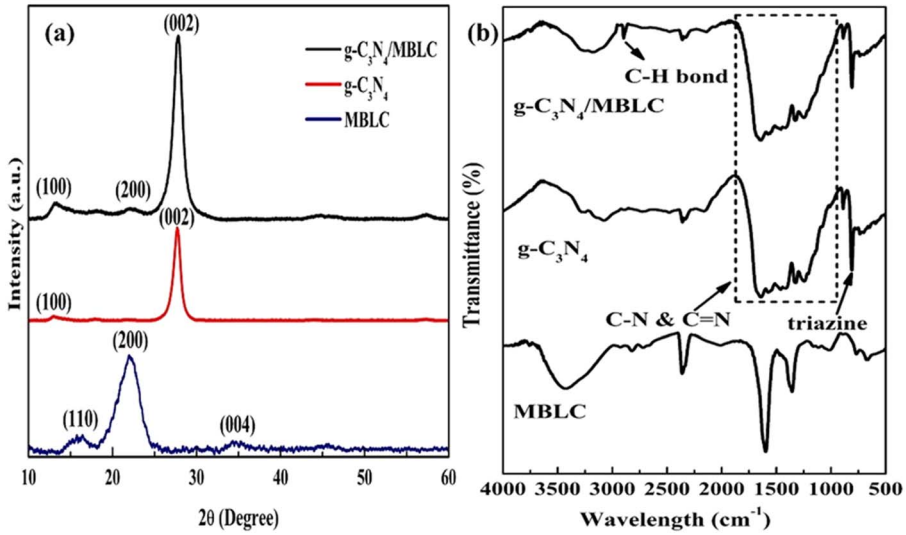

Fig. 2 (a) XRD pattern and (b) FTIR analysis of g-C_3N_4, MBLC, and g-C_3N_4/MBLC.

the triazine rings.[30,31] A distinctive infrared band was seen in the extracted cellulose at 3300–3500 cm^{-1}, which was ascribed to –OH stretching vibrations. On the other hand, C–H bending, C–OH stretching, and –OH bending vibrations were represented by the peaks at 1370, 1428, and 1645 cm^{-1}, respectively. Also, the C–O and C–O–C linkage-based backbone of the cellulose moiety was ascribed by the peaks at 1162, 1124, and 1055 cm^{-1}.[32,33] The synthesized composites exhibit preserved characteristic bands of g-C_3N_4, suggesting that the addition of extracted cellulose minimally impacted the chemical structure and configuration of g-C_3N_4. Notably, the introduction of pyrolytic cellulose resulted in new transmittance peak at 2890 cm^{-1}, corresponding to symmetric C–H vibrations. This observation further supports the formation of a heterojunction

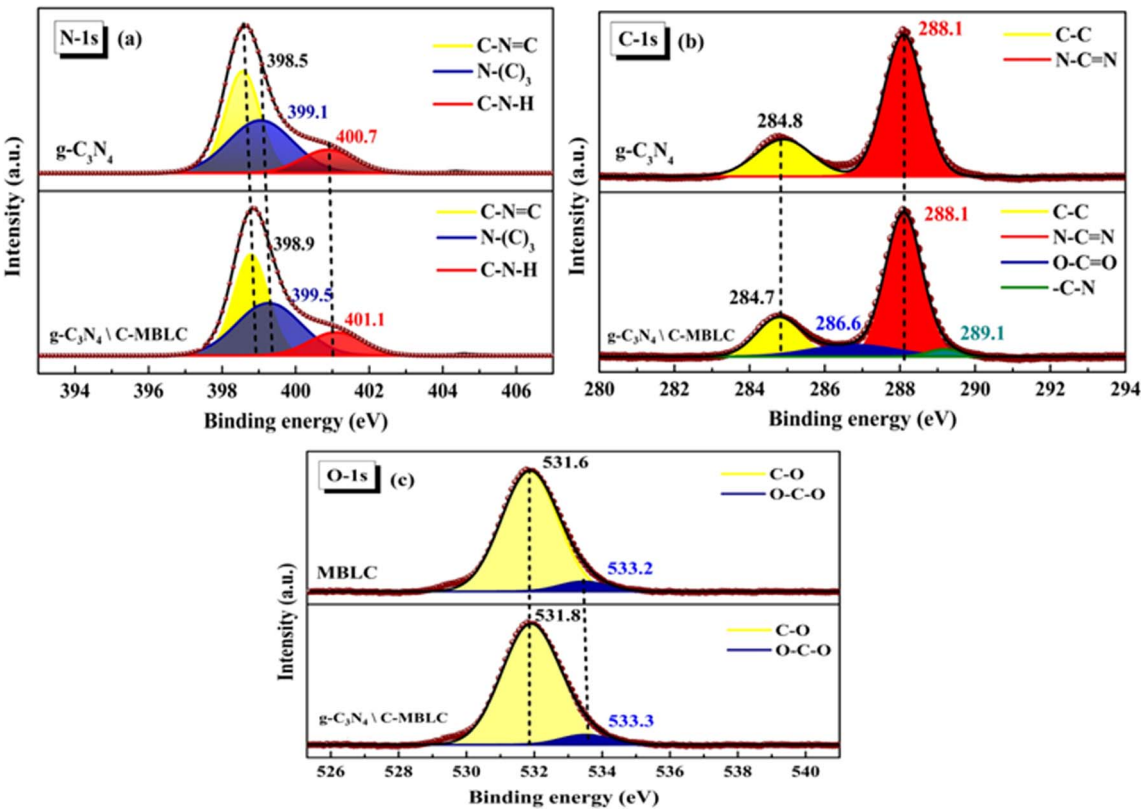

Fig. 3 XPS scan of (a) N 1s and (b) C 1s and (c) O 1s.

and the influence of melamine and cellulose interaction on g-C_3N_4 formation. The successful synthesis of the composite is evidenced by the presence of similar characteristic bands from both pure components in the final product, confirming the integration of the materials.

Fig. 3 presents the results of X-ray photoelectron spectroscopy (XPS) analysis, which was utilized to explore the chemical composition and states of both the pristine and fabricated composite materials. The N 1s XPS spectral scan exhibited peaks at 398.5 and 399.0 eV, which can be assigned to the C–N=C units of the triazine series and C(N–(C)$_3$) of the aromatic Nitrogen, respectively.[34] The peak at 400.7 eV corresponds to the C–N–H units of amino groups.[21] It is noteworthy that a subtle shift was observed in the composite, indicating potential modifications to the g-C_3N_4 skeleton due to the effect of extracted cellulose. Furthermore, Fig. 3(b) presents the spectral analysis of C 1s of the neat and synthesized composite. The 284.8 and 288.1 peaks are attributed to sp^2-carbon and C–N in the typical aromatic C_3N_4 unit.[35] Interestingly, additional peaks located at 286.6 and 289.1 eV, associated with C–O and O=C–O, were detected in the synthesized composite (g-C_3N_4/C-MBLC), providing additional evidence of the influence of the extracted cellulose on the g-C_3N_4 skeleton.[34,36] The formation of the O=C–O bond also suggests cellulose may impact the alteration of the terminal group of the g-C_3N_4 during the polymerization process.[21,37] The C 1s spectral scan of MBLC, also provided in Fig. S1,† confirmed the two peaks at 286.6 and 289.1 eV can be ascribed to C–O and O–C=O groups. Furthermore, the O 1s spectral scan (Fig. 3(c)) of the synthesized composite exhibited peaks at 531.8 and 533.3 eV, which correspond to the insertion of O from MBLC during the synthesis process (C–O and O–C–O moieties) of the composite.[26]

3.2. Theoretical analysis

DFT and TD-DFT methods were employed on the g-C_3N_4 and the synthesized g-C_3N_4/C-MBLC composite to estimate electronic distributions and their impact on the photocatalytic performance.[27] The optimized molecular structure, variation in the lowest unoccupied molecular orbitals (LUMO) and highest occupied molecular orbitals (HOMO), and energy gap of the pristine and synthesized composite are depicted in Fig. 4 and Table 1. The HOMO and LUMO structure of cellulose was provided in Fig. S2.† HOMO and LUMO energies are determined for g-C_3N_4 and g-C_3N_4/C-MBLC composite prior to and following complexation. The C–N bond in aromatic rings exhibits a length of 1.328 Å, while the same bond between the aromatic ring measures approximately 1.40 Å. Within the central ring of g-C_3N_4, the N–C–N bond angle is 122°, and the dihedral angle between the C–N–C–N bond is 168.8°. These calculated bond and angle characteristics for pure g-C_3N_4 were consistent with existing literature.[33] In the composite structure, the bond lengths and angles of the g-C_3N_4 portion remained intact. From the Table 1 parameter, the adsorption energy was calculated to be −7.54 eV, suggesting robust interactions between the pristine components. This high interaction contributes to enhanced stability within the synthesized composite material.[15]

Table 1 Parameters Including the HOMO–LUMO energies, energy gap of g-C_3N_4, MBLC, and g-C_3N_4/C-MBLC composite

Parameters	g-C_3N_4 (eV)	MBLC (eV)	g-C_3N_4/C-MBLC (eV)
E_{HOMO}	−6.6461	−6.2096	−6.1971
E_{LUMO}	−4.1723	1.2383	−3.8232
E_g	2.47	7.44	2.37

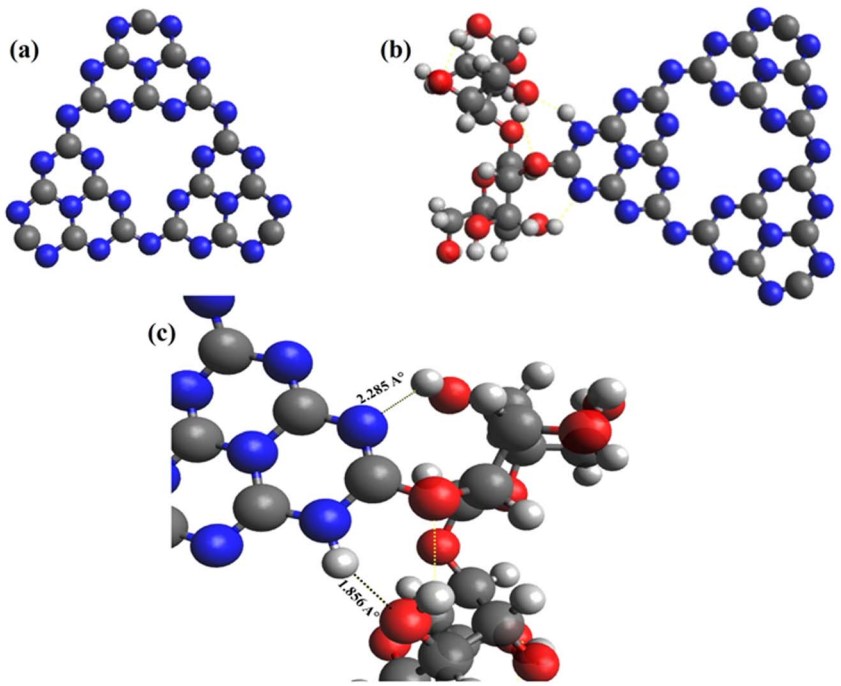

Fig. 4 Optimized geometry of (a) g-C_3N_4 and (b) g-C_3N_4/C-MBLC composite and (c) interaction between g-C_3N_4 and MBLC.

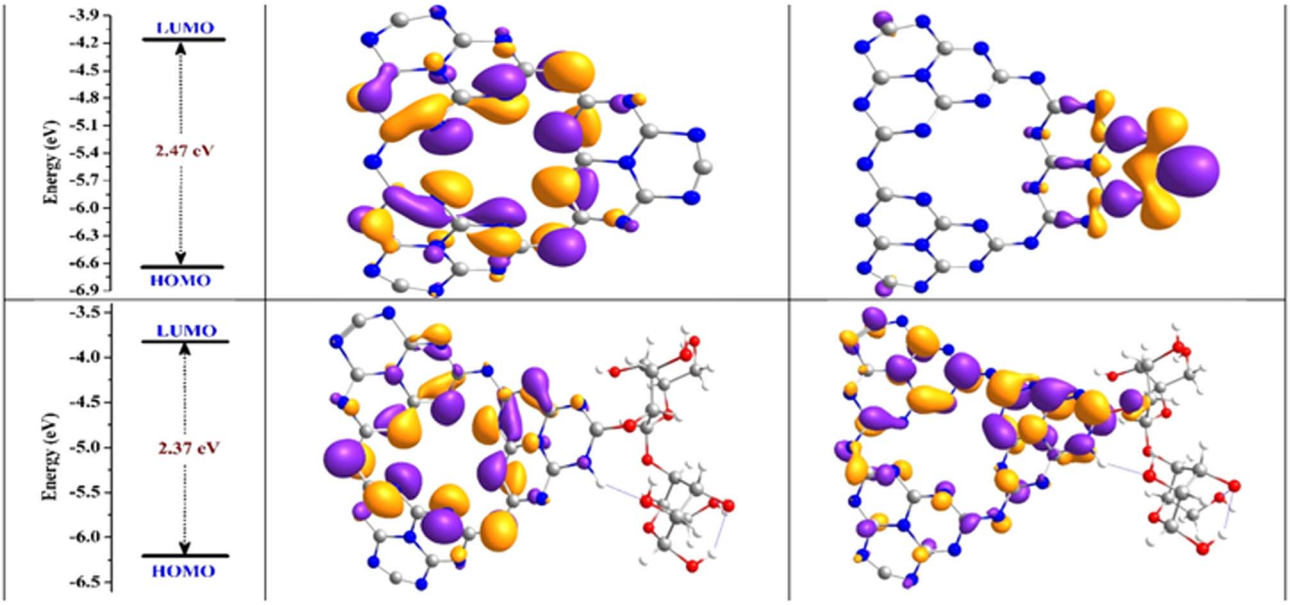

Fig. 5 Graphical representation of changes in HOMO–LUMO gaps, HOMO and LUMO of g-C_3N_4 and g-C_3N_4/C-MBLC composite.

The HOMO and LUMO energies for g-C_3N_4 are −6.6461 and −4.1723 eV, respectively, while those for the g-C_3N_4/C-MBLC composite are −6.1971 and −3.8232 eV, respectively. g-C_3N_4 exhibits a direct band gap of 2.47 eV, which reduces to 2.37 eV in the g-C_3N_4/C-MBLC composite.[27] Studies indicate that appropriate complexation can effectively decrease E_g, thus enhancing material reactivity (Fig. 5). The observed reduction in energy gap implies substantial intramolecular charge transfer within the molecule, contributing to enhanced photocatalytic performance.[38] Moreover, the E_g decrease post-composite synthesis suggests the interaction between the neat materials leads to the formation of new molecular orbitals distant from the Fermi level.[38,39] This finding also indicates that the g-C_3N_4/C-MBLC composite demonstrates superior photocatalytic stability compared to g-C_3N_4. Fig. 5 illustrates the dispersion of HOMO and LUMO, in Prior to complexation, both HOMO and LUMO are dispersed across the entire g-C_3N_4 surface. Following complexation, in the synthesized composite, the HOMO e^- density delocalized between the g-C_3N_4 and the cellulose surface, while in the LUMO the relocation of e^- density is more on the g-C_3N_4 matrix than the cellulose moiety. The E_g variation and orbital redistribution facilitate charge migration between interacting moieties. Ultimately, the post-complexation charge transfer results from electron reorganization in g-C_3N_4 and g-C_3N_4/C-MBLC composite, which is crucial for minimizing the recombination of photoinduced charge entities.

3.3. Morphological and elemental analysis

The microstructure and morphology of prepared g-C_3N_4, MBLC, and g-C_3N_4/C-MBLC composite are shown by SEM analysis in Fig. 6. The SEM image of g-C_3N_4 illustrates the ruffled monolayer structure (Fig. 6(a)).[40] The surface morphology of the composite preserves both the fibrillar cellulose structure and the uniformly dispersed layer structure of g-C_3N_4 nanosheets, as shown by the SEM images in Fig. 6(c). Hence, the morphology of the synthesized composite confirms the development of a heterojunction interface between the g-C_3N_4 with extracted cellulose moiety.[41] The EDAX analysis (Fig. 6(d)) confirms the presence of all the elements in the synthesized composite.

3.4. BET studies

As the surface area plays a pivotal role in the photodegradation activity, Fig. S3† presents the nitrogen adsorption–desorption isotherms, illustrating the materials' surface area and porosity. The isotherm analysis revealed that the g-C_3N_4/C-MBLC composite exhibited a considerably larger surface area (37.87 $m^2\ g^{-1}$) than pure g-C_3N_4 (14.022 $m^2\ g^{-1}$), as demonstrated by the greater adsorption quantity and pore size distribution. Analysis of the pore-size distribution reveals that the synthesized composite has a pore diameter of approximately 19.842 nm, while the pristine g-C_3N_4 exhibits a pore diameter of about 3.677 nm (Fig. S3(b)†). Both the pure and synthesized materials display hysteresis loops ranging from 0.7 to 1.0, indicating that they possess mesoporous properties. These assessments are crucial for comprehending the formation and effectiveness of heterojunctions, as outlined in the mechanism section. The heterojunction merges the advantages of different materials, improving charge separation and transfer. The composite's high surface area, as indicated by the isotherms and huge porosity, offers more active sites for photocatalytic reactions. This combination likely leads to enhanced photocatalytic performance of the synthesized catalyst.

3.5. UV-DRS spectral analysis and PL spectroscopy

Fig. 7(a) demonstrates the application of UV-visible diffuse reflectance spectroscopy (DRS) in assessing the band gap width

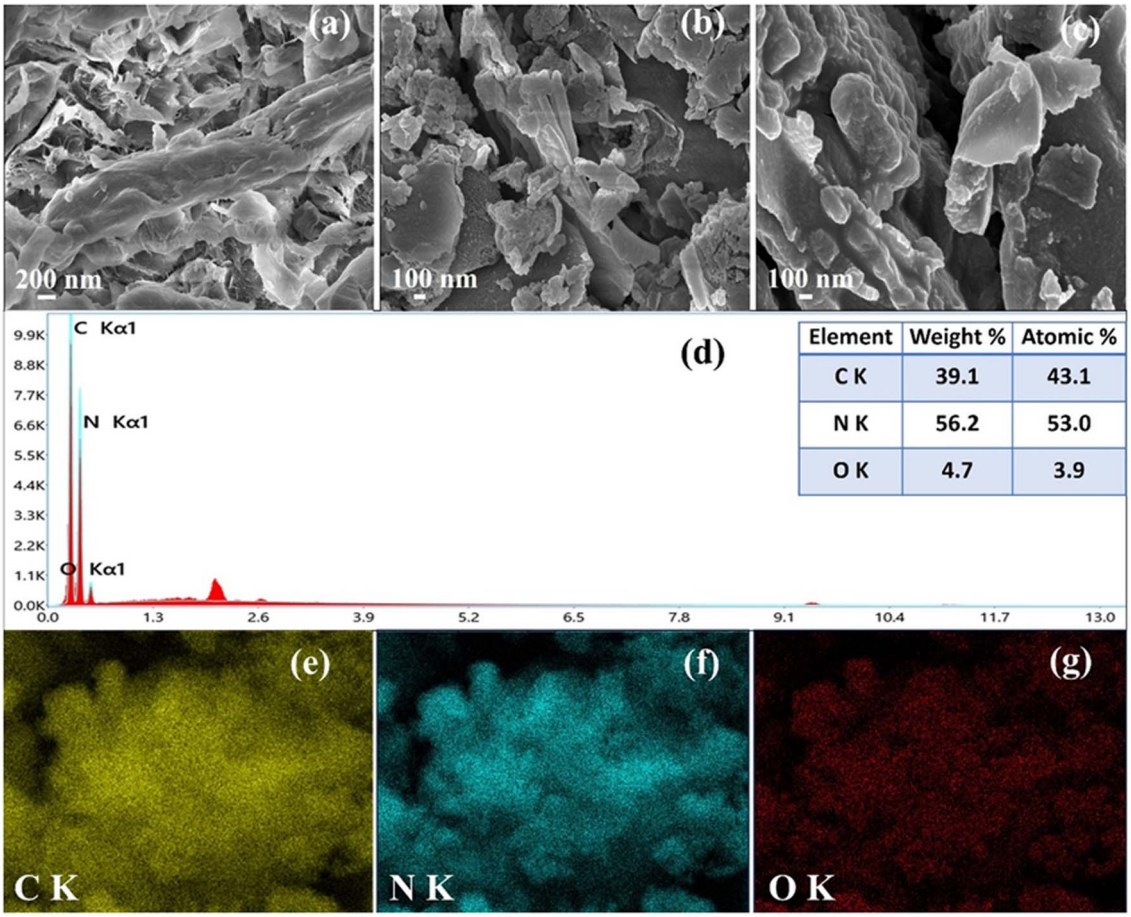

Fig. 6 SEM morphological analysis of (a) MBLC (b) g-C_3N_4 (c) g-C_3N_4/C-MBLC (d) EDS of g-C_3N_4/C-MBLC and (e–g) elemental mapping of g-C_3N_4/C-MBLC (C, N and O).

and light absorption characteristics of g-C_3N_4 and g-C_3N_4/C-MBLC composite catalysts. The findings reveal that incorporating a small amount of g-C_3N_4 into Cellulose substantially improves visible light absorption. Pure g-C_3N_4 shows strong absorption between ~200–460 nm wavelengths. In the synthesized composite, the absorption edge experiences a red shift relative to g-C_3N_4, highlighting the interaction between g-C_3N_4 and MBLC. This shift is beneficial for enhancing the efficiency of light utilization in the degradation of MB and RhB dyes. The band gap energy was calculated using the standard Tauc's method, represented by eqn (4).

$$\alpha h\nu = A(h\nu - E_g)_n \quad (4)$$

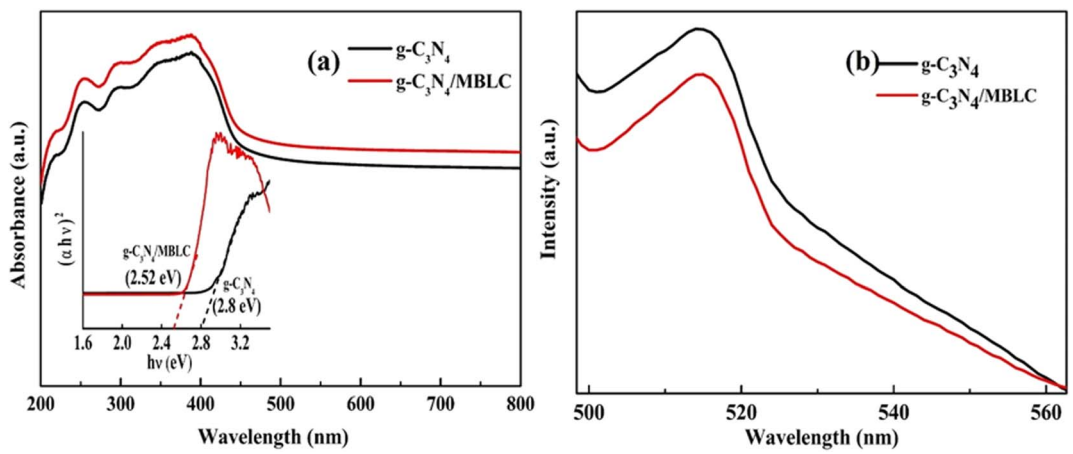

Fig. 7 (a) UV-vis-DRS, and (b) PL of the as-synthesized g-C_3N_4 and g-C_3N_4/C-MBLC composite.

For the pure samples, g-C_3N_4 displayed a band gap of 2.7 eV, while the composite exhibited 2.54 eV.[26,42] The narrower band gap of the synthesized catalyst compared to its neat component suggests enhanced visible light response and improved transferability of photogenerated carriers.

The efficiency of the photodegradation process is significantly affected by the decrease in recombination of photogenerated charge carriers. To confirm the visible light responsiveness of the synthesized catalyst, a photoluminescence (PL) spectral analysis was conducted at an excitation wavelength of 460 nm (Fig. 7(b)). The PL graph results showed that the g-C_3N_4/C-MBLC catalyst exhibited a lower PL intensity compared to the pure g-C_3N_4 sample. This observation was attributed to the well-distributed and extensive surface areas of g-C_3N_4 in the hybrid composite. The integration of finely dispersed g-C_3N_4 within the cellulose moiety produces numerous active sites, which aids in reducing charge carrier recombination and effectively enhances the photocatalytic performance of the composite.

3.6. Photodegradation activity

To better understand the overall photocatalytic process, the adsorption of RhB and MB dyes on the catalyst was evaluated prior to visible light exposure. The adsorption study was conducted using dye concentrations ranging from 10 to 70 mg L^{-1}, as shown in Fig. 8(a and b) Adsorption reached its peak within 60 minutes and plateaued at 120 minutes. As illustrated in Fig. 8(c–e), the adsorption data aligned well with both the Langmuir isotherm and pseudo-first-order kinetic models. The Langmuir isotherm model suggested a monolayer adsorption mechanism. The Freundlich adsorption isotherm and pseudo-second-order kinetics model were provided in Fig. S4.† Tables S1 and S2† provide the linear kinetic relationship between the experimental and calculated analysis. Zeta potential measurements further supported the adsorption data through surface charge evaluation. The isoelectric point was determined to be at pH = 5.34, indicating a negatively charged surface potential, which explained the minimal adsorption of cationic dyes at the working pH of 5.56 (Fig. S5†). Moreover, the process of photocatalytic degradation mainly takes place through the formation of reactive radicals. Consequently, the photocatalytic activity is not constrained by the negative zeta potential, as the reaction is primarily driven by radicals rather than direct electrostatic attraction.

Under visible light illumination, the photocatalytic degradation of RhB and MB dye was studied using the synthesized materials, g-C_3N_4, cellulose, and g-C_3N_4/Cellulose (Fig. 9). The suspension was agitated for 60 minutes in the dark before being exposed to light illumination to achieve adsorption–desorption equilibria. The efficiency of the materials in both light and dark circumstances was not notable without the catalyst which indicates the stability of the dye towards degradation, whereas upon irradiation of light in the addition of catalyst, the photodegradation occurs swiftly. The photodegradation efficacy of synthesized composite and neat samples in degrading organic dyes at different concentrations is shown in Fig. 9(a and b).

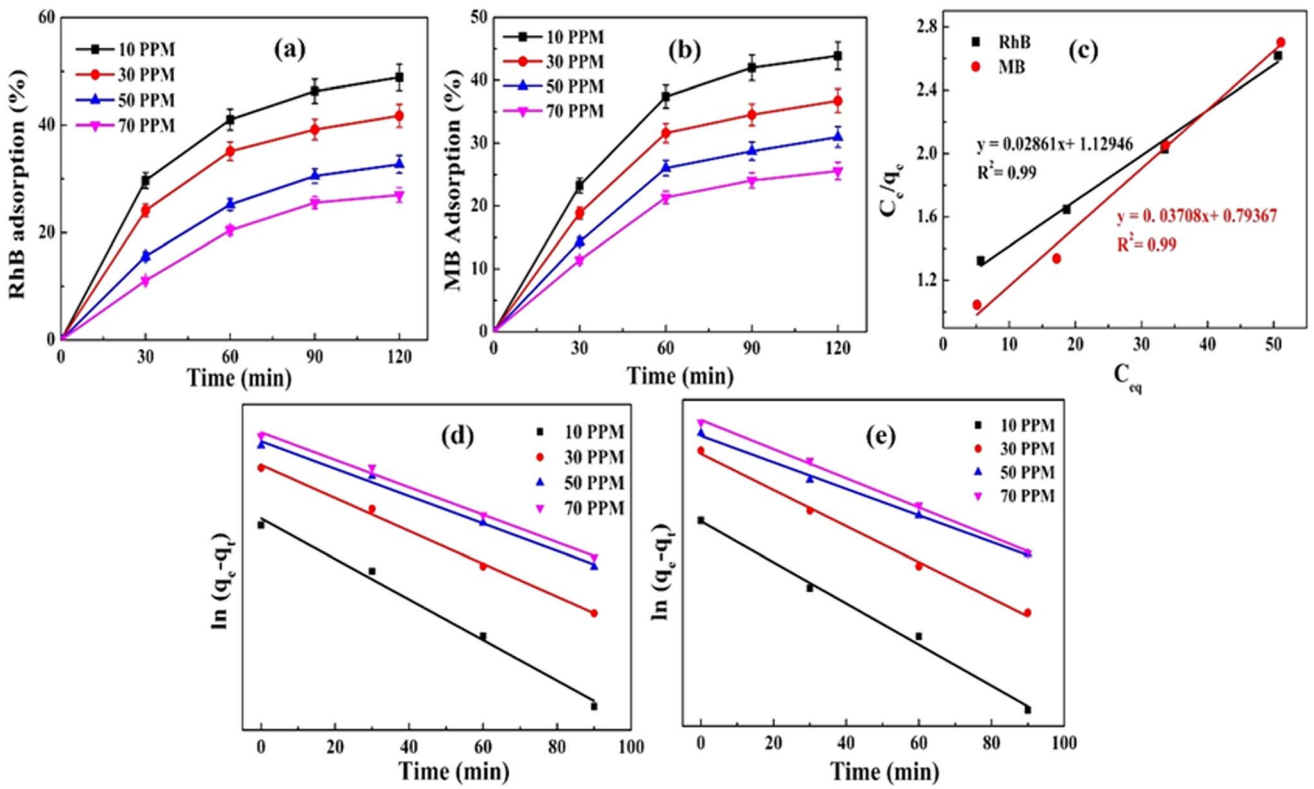

Fig. 8 (a and b) Adsorption of RhB and MB dyes onto g-C_3N_4/C-MBLC, (c) Linear plot of Langmuir isotherm model, and (d and e) Linear plots of pseudo-first-order kinetic models respectively at different initial dye concentrations.

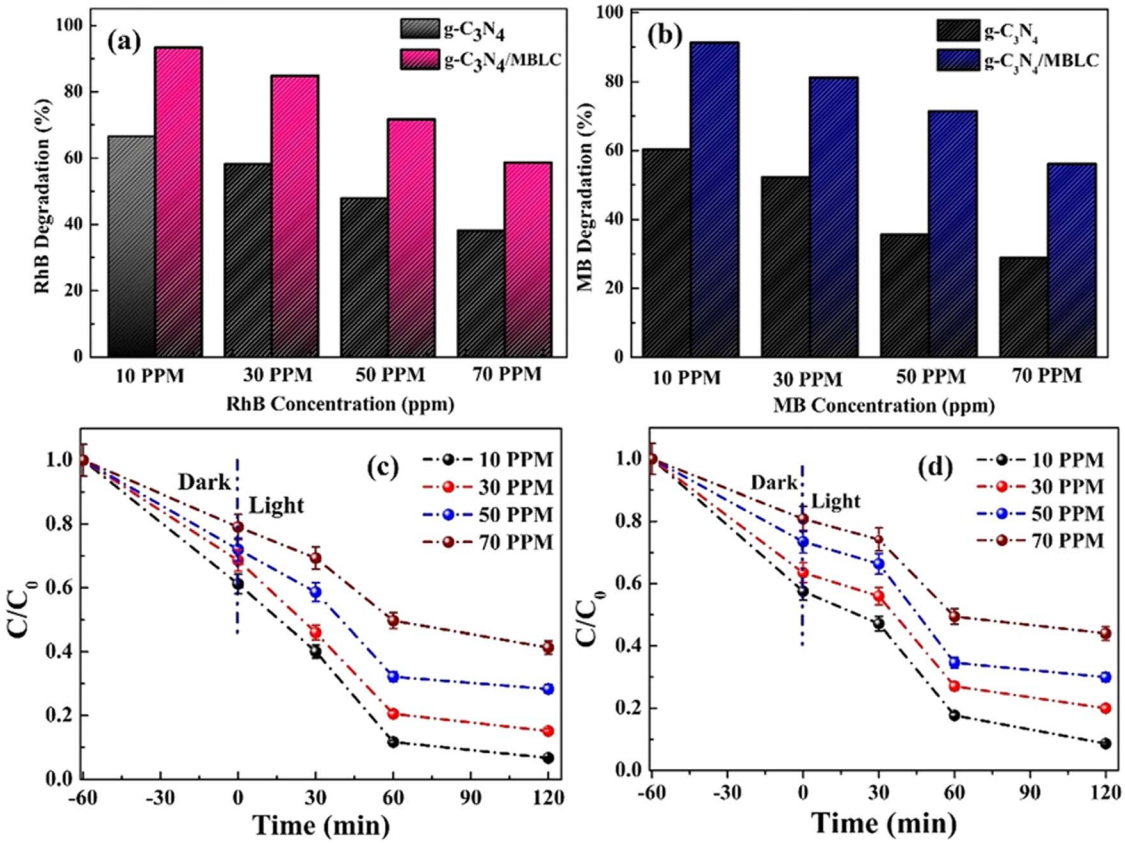

Fig. 9 (a and b) Comparative photodegradation analysis of RhB and MB dyes using g-C_3N_4, MBLC, and g-C_3N_4/C-MBLC at 30 PPM CONC. (c and d) Effect of illumination time and at different initial dye concentrations by g-C_3N_4/C-MBLC respectively.

According to the experimental study, for both dyes (RhB and MB), the synthesized composite exhibited up to 30% higher photocatalytic activity than the bare samples. Further, the photocatalytic efficacy of the composite has been analyzed by taking various concentrations of dye solutions (10–70 ppm) in different time intervals (Fig. 9(c and d)). Based on the analysis, within 120 minutes of light exposure to radiation, the as-synthesized material could completely degrade 30 mg L^{-1} of cationic dyes. With the rise in the concentration of dye solution, more aggregation of molecules occurs at the photocatalytic active sites. This aggregation of molecules perturbs the visible light transmission efficacy, ultimately reducing the generation of charge carriers, thus the photodegradation rate also decreases.

Fig. 10(a and b) displays the UV-vis spectrum of the RhB and MB dyes and the photocatalytic degradation performance of the synthesized catalyst under visible light irradiation. The graph shows that upon visible light illumination, the absorption peak intensity reduces gradually with time. This reveals that with exposure to visible light, the oxidative degradation occurred. However, a subtle shift in the UV-vis spectra of RhB dye was detected within the initial 60 minutes, suggesting a cleavage in the dye molecule's conjugated chromophore structure. Beyond this timeframe, the shift becomes more evident, likely due to the *N*-de-ethylation of the RhB molecule by oxidizing agents formed during the photodegradation process. This observed shift in the absorption maxima for RhB dye aligns with findings from previous photocatalytic studies.[22,43] The inset in Fig. 10(a) clearly illustrates the color change of the RhB solution over the 120 minutes degradation period.

Graphing the relationship between the light irradiation period and $\ln(C_0/C)$ (Fig. 10(c and d)) specifies that the oxidation of dyes follows the first-order reaction, and its kinetic equation is shown below.

$$\ln\left(\frac{C_0}{C}\right) = kt \quad (5)$$

Here t is the duration of light illumination, k is the first-order rate of reaction constant, and C_0 and C are the dye's maximum and preliminary dosages, respectively. The determined rate constants (k) were 0.015, 0.010, 0.007, and 0.005 min^{-1} for Rhodamine B (RhB) concentrations of 10, 30, 50, and 70 mg L^{-1}, respectively. A comparable declining pattern was noted for Methylene Blue (MB) dyes, with k values of 0.014, 0.009, 0.006, and 0.004 min^{-1} respectively.

3.7. GC-MS analysis

The catalytic disintegration of organic contaminants like Rhodamine B (RhB) and Methylene blue (MB) through photocatalysis produces various oxidizing agents that effectively break

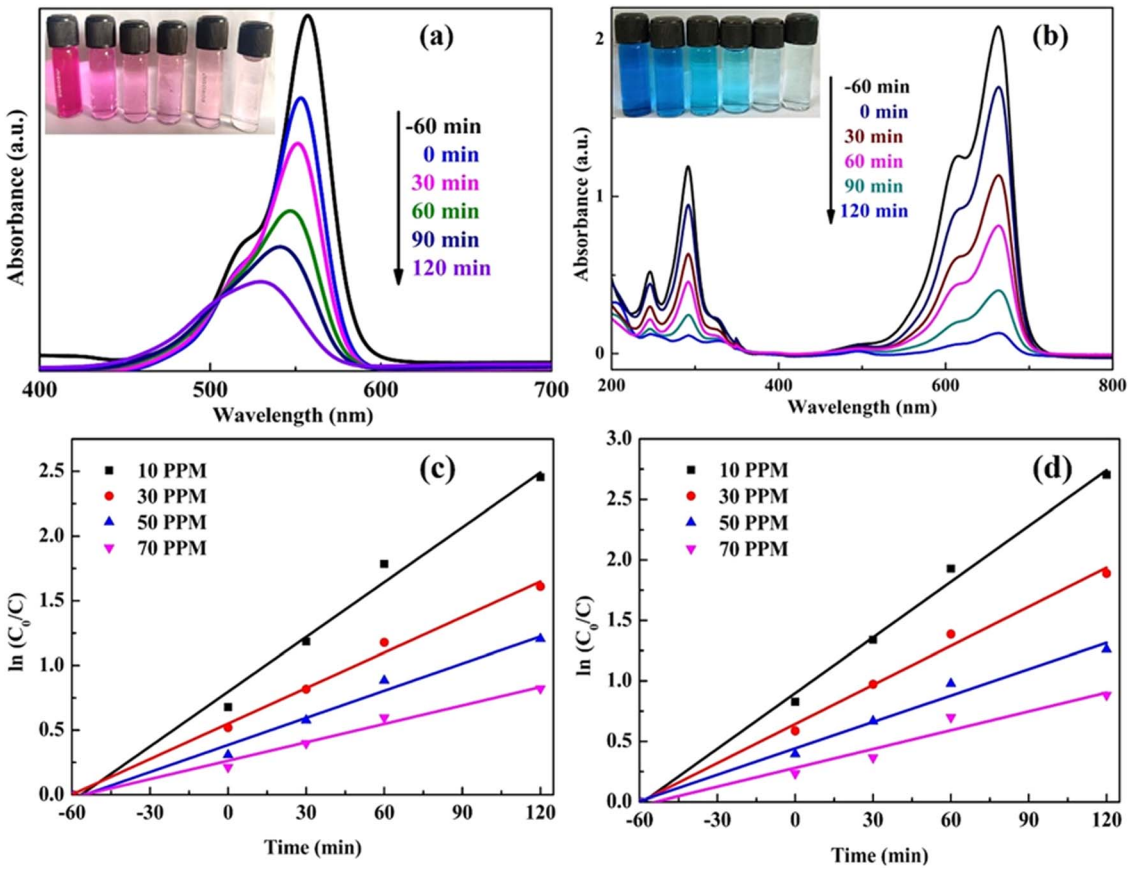

Fig. 10 (a and b) UV-vis spectra along with the inset image (c and d) kinetics profile graph of RhB and MB dyes using g-C_3N_4/C-MBLC.

down complex organic structures into smaller, less perilous molecules, such as CO_2, H_2O, and other aliphatic acids. The process involves analyzing different degraded products with their corresponding *m*/*z* values: 287, 181, 166, 156, 145, 134, 113, 97, 85, 71, 57, and 43 for RhB, and 270, 251, 177, 165, 149, 109, 99, 85, 71, 57, and 43 for MB dye (Fig. 11(a and b)). The initial intermediates formed, 6-amino-9-phenyl-3*H*-xanthen-3-iminium in RhB and (3-(dimethylamino)-7-(methylamino)phenothiazin-5-ium) in MB dye, undergo further degradation into smaller aromatic compounds (Fig. 11(c and d)). Ring-opening reactions then lead to the formation of smaller aliphatic acids and carbon dioxide as end products. Active species trapping experiments reveal that both superoxide radicals and h^+ radicals play crucial roles in breaking down both pollutants into various intermediate products and subsequently into smaller products. Specifically, the superoxide radical produced in the photocatalyst's conduction band targets dye molecules, breaking them down into aromatic intermediates and then into aliphatic acids and harmless substances. Likewise, the h^+ generated in the catalyst's valence band assists in fragmenting the dyes into non-hazardous products and minor organic components.

3.8. Scavenging activity

To gain deeper insights into the photocatalysis mechanism and the active species involved, a trapping experiment was performed using BQ, EDTA, and IPA. Under visible light exposure, these trapping agents demonstrated an inhibitory effect on the degradation of both dyes, as illustrated in Fig. 12(a). The introduction of BQ and EDTA into the MB dye solution markedly decreased the catalyst's photodegradation efficiency, with a comparable reduction observed for RhB dye in the presence of these agents. Consequently, the impact of active species on dye degradation follows the sequence $^{\bullet}OH < h^+ < {}^{\bullet}O_2^-$. This indicates that $^{\bullet}O_2^-$ and h^+ are essential in transforming harmful organic dyes into less dangerous compounds. Additionally, the presence of IPA caused a minor decrease in photodegradation efficiency, suggesting that the $^{\bullet}OH$ radical plays a minimal role in the degradation process.[21]

3.9. Plausible mechanism

Based on the outcomes of the scavenging data, a plausible photodegradation mechanism for the synthesized composite is depicted in Fig. 12(b). When a semiconductor photocatalyst is exposed to light energy equal to or surpassing its bandgap energy, electrons (e^-) transition from the valence band to the conduction band, concurrently creating holes in the valence band.[44,45] These photoinduced charge carriers can initiate redox reactions with organic substances. In the synthesized, g-C_3N_4/C-MBLC catalyst, the addition of MBLC increases the surface area and minimizes the aggregation of the g-C_3N_4 component, thereby enhancing

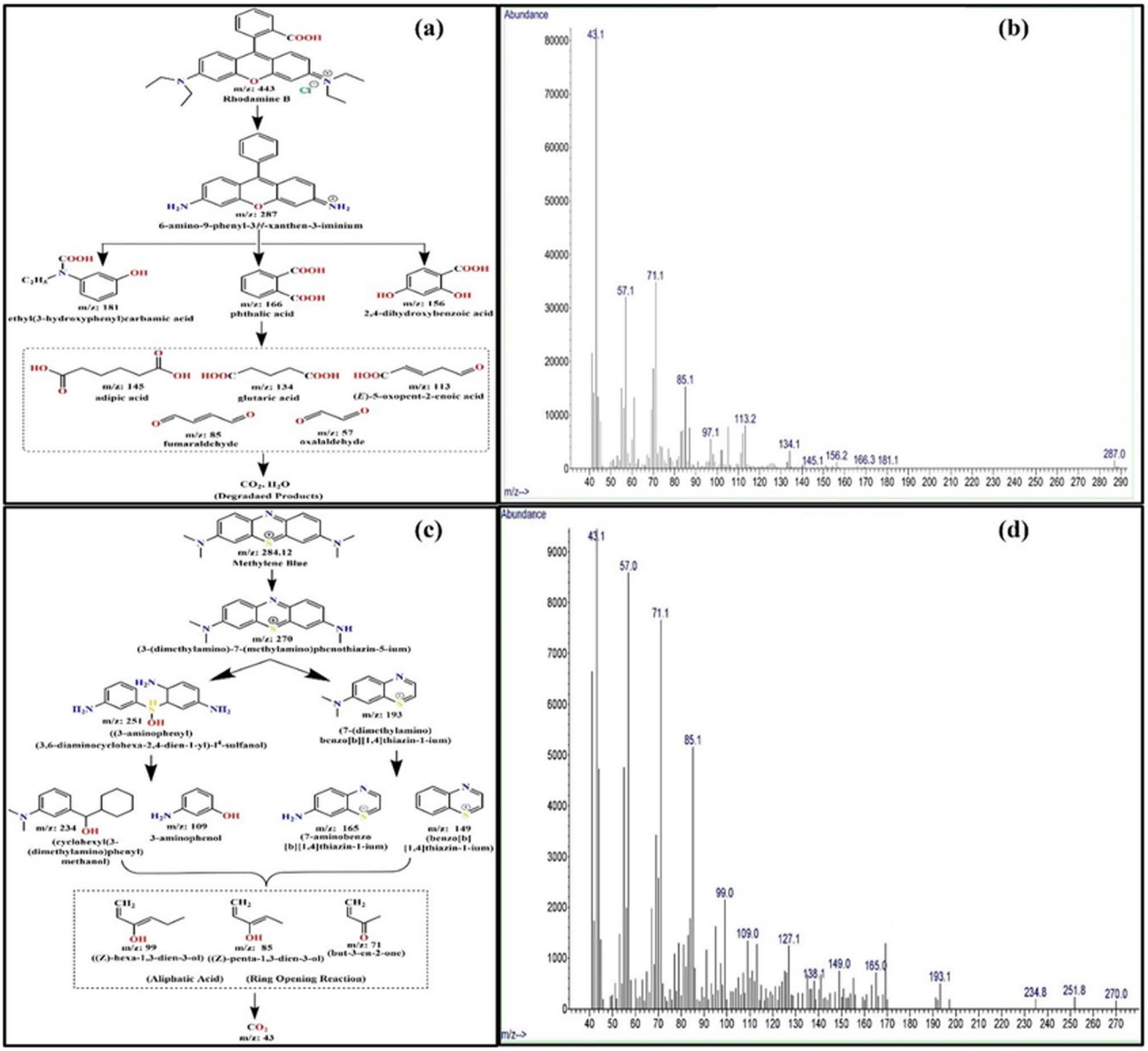

Fig. 11 GC-MS analysis of photodegradation of (a and b) RhB and (c and d) MB by g-C_3N_4/C-MBLC.

light absorption efficiency and charge migration capability. Modifying the surface aids in capturing photogenerated electrons, significantly decreasing the recombination of photoinduced charge carriers. Additionally, the hydrogen bonding and synergistic interaction between g-C_3N_4 and MBLC prevent the recombination of electron and hole pairs. This recombination inhibition is also attributed to electron transfer *via* hydrogen bonds, as confirmed by DFT analysis. This occurs because the numerous hydroxyl groups in MBLC form stronger hydrogen bonds with the amino groups of g-C_3N_4, which boost electron transfer and the conduction of photo-generated electrons, further encouraging the production of photo-generated superoxide radicals ($^{\bullet}O_2^-$), thus aiding in dye degradation.[46,47] Consequently, employing g-C_3N_4 photocatalysts under visible light, a plausible mechanism for the photodegradation of RhB and MB dyes was explored (Fig. 12(b)). Visible light stimulates the g-C_3N_4 photocatalyst, causing electron excitation from its conduction band to the valence band. Subsequently, conduction band electrons can interact with molecular O_2 to produce superoxide radicals (−1.13 eV *vs.* NHE) as the potential of the conduction band is more negative than the standard reduction potential (E ($O_2/^{\bullet}O_2^-$) = −0.33 V).[48] In contrast, the generated holes in the VB band (+1.57 eV) directly oxidize the pollutants to a greater extent as the catalyst did not possess the required potential for the oxidation of H_2O to generate $^{\bullet}$OH radicals. The following eqn (6)–(8) explains the formation of the superoxide radical on the surface of the synthesized composite followed by the degradation of the organic dyes.

$$\text{g-}C_3N_4\text{/C-MBLC} + h\nu \rightarrow e_{CB}^- + h_{VB}^+ \quad (6)$$

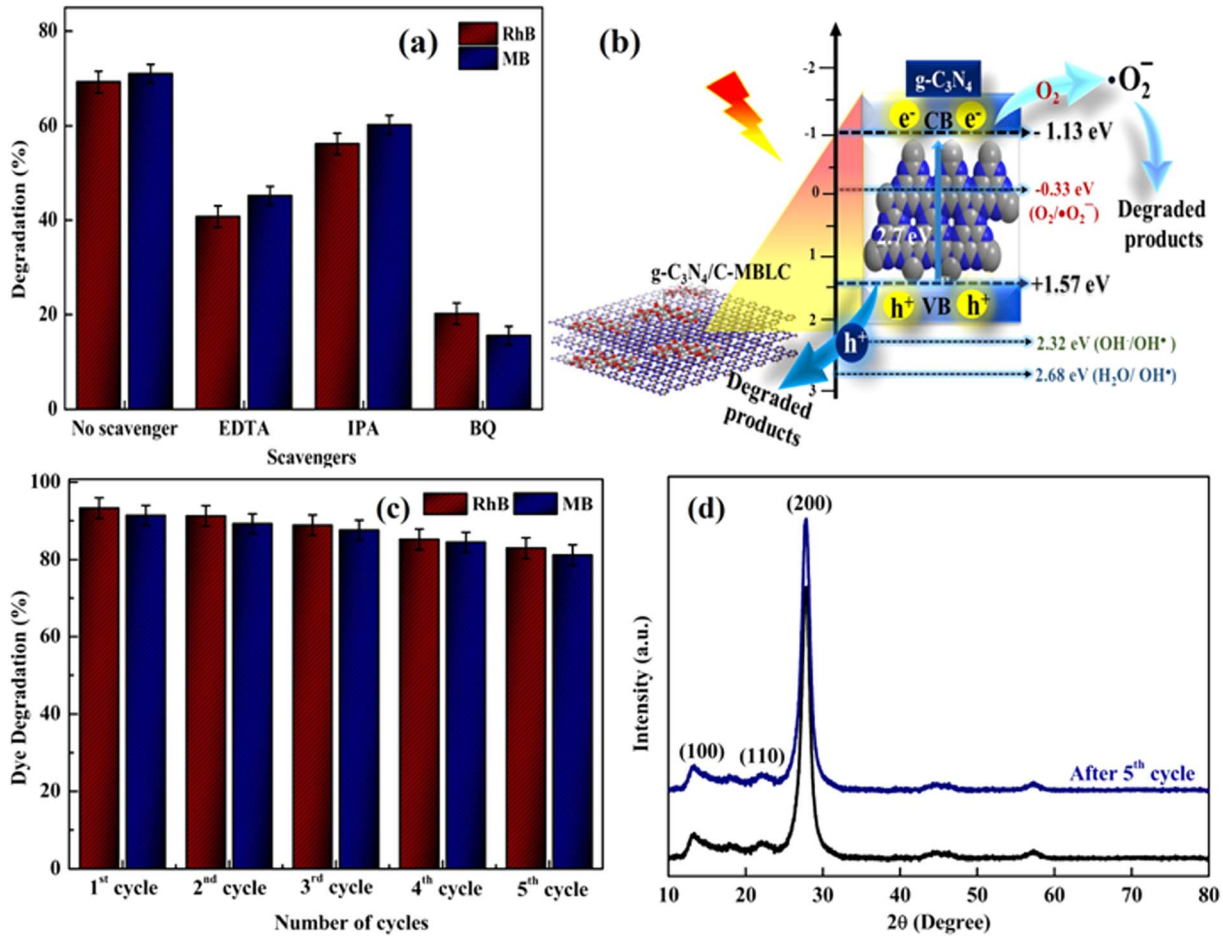

Fig. 12 (a) Scavenging activity (b) plausible mechanism (c) recyclability (d) PXRD assessment using g-C_3N_4/C-MBLC composite.

$$e^-_{CB} + O_2 \rightarrow {}^{\bullet}O_2^- \quad (7)$$

$${}^{\bullet}O_2^- + h_{VB}^+ + \text{RhB/MB} \rightarrow \text{intermediates} \rightarrow \text{degraded products} \quad (8)$$

These radicals, possessing unpaired electrons, exhibit high reactivity and instability, attacking organic impurities and breaking them down into less hazardous byproducts. Additionally, as the photoexcited charge carriers migrate in the opposite direction, that also leads to an increase in the photodegradation efficacy.

3.10. Recyclability

The durability of the synthesized g-C_3N_4/C-MBLC photocatalyst was explored by conducting degradation experiments with the same photocatalyst five times under the exact experimental circumstances, as illustrated in Fig. 12(c). The degradation percentage of both dyes did not significantly vary after five consecutive cycles. A slight decrease in the degradation percentage observed may be attributed to the formation of a hydroxide layer on the photocatalyst's surface and the loss of catalyst during stirring. The degradation rate of RhB dye dropped from 93.29% to 82.92% and MB dye from 92.06% to 83.19% throughout the recyclability test. Furthermore, XRD assessments (Fig. 10(d)) and FTIR (Fig. S6†) were also analyzed, indicating no discernible pattern changes indicating stability of the catalyst. It confirmed that the synthesized composite is stable and can be reused up to 4th cycle. Thus, the catalyst exhibited virtuous steadiness, recyclability, and reusability for RhB and MB dye degradation. A comparative photocatalytic activity of synthesized composite along with other reported literature is given in Table S3.†

4. Conclusion

This work involved the utilization of the beneficial and economically viable catalyst g-C_3N_4/C-MBLC in photocatalytic degradation investigations to eliminate the dyes RhB and MB. Based on the outcomes, it was found that the materials act as superior catalysts for removing organic dyes. The characterization also revealed an enhanced surface area of the synthesized composite than the pristine g-C_3N_4 components. Furthermore, the degradation percentage of the catalytic material was observed up to 93.35% and 92.06%. The proposed mechanism of biomass catalysts also confirmed the pivotal role of ${}^{\bullet}O_2^-$ radical for the disintegration of organic pollutants. The

synthetic composite's capacity for recycling was assessed throughout five cycles, and after that, the percentage of disintegration decreased substantially, showing that the photocatalyst remained stable. Furthermore, investigating actual sewage treatment will benefit from the use of cellulose as a biomass precursor in the synthesized composite.

Data availability

The authors declare that the data supporting the findings of this study are available in the paper and its ESI files.† If raw data files in another format are needed, they can be obtained from the corresponding author upon reasonable request.

Author contributions

Priyanka P. Mishra: conceptualization, formal analysis, investigation, writing-original draft, writing-review & editing. Diptiranjan Behera: conceptualization, methodology, writing-original draft. Sushree Suman: writing-review & editing. Nigamananda Das: formal analysis, editing. Bankim C. Tripathy: formal analysis, editing. Jagdish Kumar: formal analysis, Ajaya K. Behera: supervision, visualization, formal analysis, editing – original draft.

Conflicts of interest

The authors declare no conflict of interest.

Acknowledgements

We acknowledge the assistance of DST, Govt. of Odisha (Project No. 3444/ST), for part of this work. We are very grateful to the Department of Chemistry, Utkal University, Odisha, for allowing the smooth conduct of experiments.

References

1 S. Mustafa, H. N. Bhatti, M. Maqbool and M. Iqbal, Microalgae biosorption, bioaccumulation and biodegradation efficiency for the remediation of wastewater and carbon dioxide mitigation: Prospects, challenges and opportunities, *J. Water Process Eng.*, 2021, **41**, 102009.

2 N. H. H. Hairom, C. F. Soon, R. M. S. R. Mohamed, M. Morsin, N. Zainal, N. Nayan, C. Z. Zulkifli and N. H. Harun, A review of nanotechnological applications to detect and control surface water pollution, *Environ. Technol. Innov.*, 2021, **24**, 102032.

3 A. Getu and O. Sahu, Removal of Reactive Dye using Activated Carbon from Agricultural Waste, *J. Eng. Geol. Hydrogeol.*, 2014, **2**, 23.

4 E. M. Saggioro, A. S. Oliveira, T. Pavesi, C. G. Maia, L. F. V. Ferreira and J. C. Moreira, Use of titanium dioxide photocatalysis on the remediation of model textile wastewaters containing azo dyes, *Molecules*, 2011, **16**(12), 10370–10386.

5 S. Lin, W.-L.-J. Hasi, X. Lin, S. Han, X.-T. Lou, F. Yang, D.-Y. Lin and Z.-W. Lu, Rapid and sensitive SERS method for determination of Rhodamine B in chili powder with paper-based substrates, *Anal. Methods*, 2015, **7**, 5289–5294.

6 V. Selvaraj, T. Swarna Karthika, C. Mansiya and M. Alagar, An over review on recently developed techniques, mechanisms and intermediate involved in the advanced azo dye degradation for industrial applications, *J. Mol. Struct.*, 2021, **1224**, 129195.

7 A. S. Alshammari, A. Bagabas, N. Alarifi and R. Altamimi, Effect of the nature of metal nanoparticles on the photocatalytic degradation of rhodamine B, *Top. Catal.*, 2019, **62**, 786–794.

8 A. B. Dos Santos, F. J. Cervantes and J. B. Van Lier, Review paper on current technologies for decolourisation of textile wastewaters: perspectives for anaerobic biotechnology, *Bioresour. Technol.*, 2007, **98**, 2369–2385.

9 N. Dizge, C. Aydiner, E. Demirbas, M. Kobya and S. Kara, Adsorption of reactive dyes from aqueous solutions by fly ash: kinetic and equilibrium studies, *J. Hazard. Mater.*, 2008, **150**, 737–746.

10 N. M. Mahmoodi and Z. Mokhtari-Shourijeh, Preparation of PVA-chitosan blend nanofiber and its dye removal ability from colored wastewater, *Fibers Polym.*, 2015, **16**, 1861–1869.

11 C. Mohanty, P. P. Mishra, A. Samal, N. Das and A. K. Behera, Design of inexpensive, magnetically separable MnFe 2 O 4/poly meta-amino phenol (PmAP) heterostructure: catalyst for bisphenol A & reactive blue 19 mineralisation, *Environ. Sci. Adv*, 2024, **3**, 561–571.

12 H. Zhang, Y. Gao, S. Meng, Z. Wang, P. Wang, Z. Wang, C. Qiu, S. Chen, B. Weng and Y. M. Zheng, Metal sulfide S-scheme homojunction for photocatalytic selective phenylcarbinol oxidation, *Adv. Sci.*, 2024, **11**, 2400099.

13 W. Cheng, L. Wang, H. Lao, Y. Wei, J. Xu and B. Weng, Unraveling the Plasmonic Effect of Au in Promoting Photocatalytic H2 Generation and Organic Synthesis, *ACS Sustain. Chem. Eng.*, 2024, **12**, 17026–17034.

14 Z. Li, Q. Chen, Q. Lin, Y. Chen, X. Liao, H. Yu and C. Yu, Three-dimensional P-doped porous g-C3N4 nanosheets as an efficient metal-free photocatalyst for visible-light photocatalytic degradation of Rhodamine B model pollutant, *J. Taiwan Inst. Chem. Eng.*, 2020, **114**, 249–262.

15 H. Huang, J. Zhao, H. Guo, B. Weng, H. Zhang, R. A. Saha, M. Zhang, F. Lai, Y. Zhou, R. Z. Juan and P. C. Chen, Noble-metal-free high-entropy alloy nanoparticles for efficient solar-driven photocatalytic CO_2 reduction, *Adv. Mater.*, 2024, **36**, 2313209.

16 H. Kumar, M. Luthra, M. Punia and R. M. Singh, Co3O4/PANI nanocomposites as a photocatalytic, antibacterial and anticorrosive agent: Experimental and theoretical approach, *Colloid Interface Sci. Commun.*, 2021, **45**, 100512.

17 X. Wang, X. Liu, H. Wen, K. Guo, H. Brendon and D. Liu, A green, efficient reductive N-formylation of nitro compounds catalyzed by metal-free graphitic carbon nitride supported on activated carbon, Appl, *Catal. B Environ.*, 2023, **321**, 122042.

18 J. Wang, J. Xu, S. Zhu, Q. Wu, J. Li, Y. Gao, B. Wang, J. Li, W. Gao, J. Zeng and K. Chen, Preparation of nanocellulose in high yield via chemi-mechanical synergy, *Carbohydr. Polym.*, 2021, **251**, 117094.

19 T. C. Mokhena, E. R. Sadiku, M. J. Mochane, S. S. Ray, M. J. John and A. Mtibe, Mechanical properties of cellulose nanofibril papers and their bionanocomposites: A review, *Carbohydr. Polym.*, 2021, **273**, 118507.

20 S. Chen, W. Lu, J. Han, H. Zhong, T. Xu, G. Wang and W. Chen, Robust three-dimensional g-C3N4@ cellulose aerogel enhanced by cross-linked polyester fibers for simultaneous removal of hexavalent chromium and antibiotics, *Chem. Eng. J.*, 2019, **359**, 119–129.

21 B. He, M. Feng, X. Chen, D. Zhao and J. Sun, One-pot construction of chitin-derived carbon/g-C3N4 heterojunction for the improvement of visible-light photocatalysis, *Appl. Surf. Sci.*, 2020, **527**, 146737.

22 P. R. Anusuyadevi, A. V. Riazanova, M. S. Hedenqvist and A. J. Svagan, Floating photocatalysts for effluent refinement based on stable pickering cellulose foams and graphitic carbon nitride (g-C3N4), *ACS Omega*, 2020, **5**, 22411–22419.

23 H. Sun, L. Zheng, Y. Xi, S. Zhai, Q. An and Z. Xiao, Nickel-iron sulfide nanoparticles supported on biomass-derived N-doped hierarchical porous carbon as a robust electrode for supercapacitors, *Electrochim. Acta*, 2023, **466**, 143053.

24 Y. Chen, Z. Xiang, D. Wang, J. Kang and H. Qi, Effective photocatalytic degradation and physical adsorption of methylene blue using cellulose/GO/TiO 2 hydrogels, *RSC Adv.*, 2020, **10**, 23936–23943.

25 N. Kumar, B. Kumar, H. Gupta and A. Kumar, Development and evaluation of cellulose/graphene-oxide based composite for removing phenol from aqueous solutions, *Polymers*, 2023, **15**, 572.

26 Y. Chen, W. Shao, C. Zhou, G. Tai, G. Wu and W. Xing, Enhanced photocatalytic performance of carbon nitride through modification of edge sites with cellulose-derived carbon species for H2 evolution and tetracycline degradation, *ACS Appl. Energy Mater.*, 2023, **6**, 22.

27 M. Ilyas, A. R. Ayu, R. A. Shehzad, M. A. Khan, M. Perveen, S. Amin, S. Muhammad and J. Iqbal, A DFT approach for finding therapeutic potential of two dimensional (2D) graphitic carbon nitride (GCN) as a drug delivery carrier for curcumin to treat cardiovascular diseases, *J. Mol. Struct.*, 2022, **1257**, 132547.

28 A. Thomas, A. Fischer, F. Goettmann, M. Antonietti, J.-O. Müller, R. Schlögl and J. M. Carlsson, Graphitic carbon nitride materials: variation of structure and morphology and their use as metal-free catalysts, *J. Mater. Chem.*, 2008, **18**, 4893.

29 C. Trilokesh and K. B. Uppuluri, Isolation and characterization of cellulose nanocrystals from jackfruit peel, *Sci. Rep.*, 2019, **9**, 16709.

30 G. Di, Z. Zhu, H. Zhang, J. Zhu, Y. Qiu, D. Yin and S. Küppers, Visible-light degradation of sulfonamides by Z-scheme ZnO/g-C3N4 heterojunctions with amorphous Fe2O3 as electron mediator, *J. Colloid Interface Sci.*, 2019, **538**, 256–266.

31 T. Fan, C. Chen, Z. Tang, Y. Ni and C. Lu, Synthesis and characterization of g-C3N4/BiFeO3 composites with an enhanced visible light photocatalytic activity, *Mater. Sci. Semicond. Process.*, 2015, **40**, 439–445.

32 Y. Hao, Y. Cui, J. Peng, N. Zhao, S. Li and M. Zhai, Preparation of graphene oxide/cellulose composites in ionic liquid for Ce (III) removal, *Carbohydr. Polym.*, 2019, **208**, 269–275.

33 J. Tao, J. Yang, C. Ma, J. Li, K. Du, Z. Wei, C. Chen, Z. Wang, C. Zhao and X. Deng, Cellulose nanocrystals/graphene oxide composite for the adsorption and removal of levofloxacin hydrochloride antibiotic from aqueous solution, *R. Soc. Open Sci.*, 2020, **7**, 200857.

34 A. Li, Q. Cao, G. Zhou, B. V. K. J. Schmidt, W. Zhu, X. Yuan, H. Huo, J. Gong and M. Antonietti, Three-phase photocatalysis for the enhanced selectivity and activity of CO2 reduction on a hydrophobic surface, *Angew. Chem., Int. Ed.*, 2019, **58**, 14549–14555.

35 W. Ho, Z. Zhang, W. Lin, S. Huang, X. Zhang, X. Wang and Y. Huang, Copolymerization with 2, 4, 6-triaminopyrimidine for the rolling-up the layer structure, tunable electronic properties, and photocatalysis of g-C3N4, *ACS Appl. Mater. Interfaces*, 2015, **7**, 5497–5505.

36 W. Wang, H. Zhang, S. Zhang, Y. Liu, G. Wang, C. Sun and H. Zhao, Potassium-ion-assisted regeneration of active cyano groups in carbon nitride nanoribbons: visible-light-driven photocatalytic nitrogen reduction, *Angew. Chem., Int. Ed.*, 2019, **58**, 16644–16650.

37 X. Li, X. Sun, L. Zhang, S. Sun and W. Wang, Efficient photocatalytic fixation of N2 by KOH-treated g-C3N4, *J. Mater. Chem. A*, 2018, **6**, 3005–3011.

38 M. Asif, N. Kosar, H. Sajid, S. Qureshi, M. A. Gilani, K. Ayub, M. Arshad, M. Imran, M. H. S. A. Hamid, I. Bayach, N. S. Sheikh and T. Mahmood, Exploring the Sensing Potential of g-C3N4 versus Li/g-C3N4 Nanoflakes toward Hazardous Organic Volatiles: A DFT Simulation Study, *ACS Omega*, 2024, **9**(3), 3541–3553.

39 A. S. Rad and K. Ayub, Adsorption of thiophene on the surfaces of X12Y12 (X= Al, B, and Y= N, P) nanoclusters; A DFT study, *J. Mol. Liq.*, 2017, **238**, 303–309.

40 H. Huo, Y. Li, S. Wang, S. Tan, X. Li, S. Yi and L. Gao, Construction of highly active Zn3In2S6 (110)/g-C3N4 system by low temperature solvothermal for efficient degradation of tetracycline under visible light, *Int. J. Mol. Sci.*, 2022, **23**, 13221.

41 P. Krishnamachari, R. Hashaikeh and M. Tiner, Modified cellulose morphologies and its composites; SEM and TEM analysis, *Micron*, 2011, **42**, 751–761.

42 C. Mohanty, A. Samal and N. Das, Concurrent photoreforming of polyethylene into commercial chemicals and hydrogen generation utilizing g-C_3N_4/Co_3O_4 Z-scheme heterostructure: A waste-to-wealth concept, *Int. J. Hydrog. Energy*, 2024, **61**, 84–93.

43 Y. Cui, S. M. Goldup and S. Dunn, Photodegradation of Rhodamine B over Ag modified ferroelectric BaTiO 3 under simulated solar light: pathways and mechanism, *RSC Adv.*, 2015, **5**, 30372–30379.

44 P. Niu, L. Zhang, G. Liu and H. Cheng, Graphene-like carbon nitride nanosheets for improved photocatalytic activities, *Adv. Funct. Mater.*, 2012, **22**, 4763–4770.

45 S. P. Pattnaik, A. Behera, S. Martha, R. Acharya and K. Parida, Facile synthesis of exfoliated graphitic carbon nitride for photocatalytic degradation of ciprofloxacin under solar irradiation, *J. Mater. Sci.*, 2019, **54**, 5726–5742.

46 A. Li, Z. Zhang, C. Feng, T. Zhang, F. Liu, H. Na and J. Zhu, Fabrication of a Nanosized g-C3N4-Loaded Cellulose Microfiber Bundle to Induce Highly Efficient Water Treatment via Photodegradation, *Langmuir*, 2023, **39**, 16657–16667.

47 H. Huang, J. Zhao, B. Weng, F. Lai, M. Zhang, J. Hofkens, M. B. J. Roeffaers, J. A. Steele and J. Lon, Site-Sensitive Selective CO2 Photoreduction to CO over Gold Nanoparticles, *Angewandte Chmie*, 2022, **61**, e202204563.

48 Y. H. Chiu, T. F. M. Chang, C. Y. Chen, M. Sone and Y. J. Hsu, Mechanistic insights into photodegradation of organic dyes using heterostructure photocatalysts, *Catalysts*, 2019, **9**(5), 430.